

See discussions, stats, and author profiles for this publication at: <https://www.researchgate.net/publication/281404508>

High and Anisotropic Carrier Mobility in Experimentally Possible Ti_2CO_2 (MXene) Monolayer and Nanoribbons

ARTICLE *in* NANOSCALE · SEPTEMBER 2015

Impact Factor: 7.39 · DOI: 10.1039/C5NR04717J

READS

5

5 AUTHORS, INCLUDING:



Xu Zhang

Nankai University

7 PUBLICATIONS 9 CITATIONS

SEE PROFILE



Yu Jing

Nankai University

14 PUBLICATIONS 312 CITATIONS

SEE PROFILE



Zhen Zhou

Nankai University

212 PUBLICATIONS 6,964 CITATIONS

SEE PROFILE



Cite this: *Nanoscale*, 2015, 7, 16020

High and anisotropic carrier mobility in experimentally possible Ti_2CO_2 (MXene) monolayers and nanoribbons†

Xu Zhang, Xudong Zhao, Dihua Wu, Yu Jing and Zhen Zhou*

MXene, a new kind of two-dimensional (2D) material, has a unique combination of excellent physical and chemical properties. *Via* computations on density functional theory and deformation potential theory, we investigated the electronic structure and predicted the carrier mobility of Ti_2CO_2 (a typical MXene) monolayers and nanoribbons. The Ti_2CO_2 monolayer is a semiconductor with a band gap of 0.91 eV, and the hole mobility in the monolayer reaches 10^4 orders of magnitude along both *x* and *y* directions, which is much higher than that of MoS_2 , while the electron mobility is about two orders of magnitude lower. The dramatic difference between the hole and electron mobilities also exists in nanoribbons. Moreover, our results suggest that width controlling and edge engineering would be effective in adjusting the carrier mobility of Ti_2CO_2 nanoribbons, and endow experimentally available Ti_2CO_2 with wide applications to field-effect transistors and photocatalysts.

Received 14th July 2015,
Accepted 27th August 2015

DOI: 10.1039/c5nr04717j

www.rsc.org/nanoscale

1. Introduction

Since the experimental realization of graphene,¹ two-dimensional (2D) materials have attracted intensive interest for nanoscale electronic and photonic devices due to their unique combination of excellent physical and chemical properties. Thus, many atomic-layer systems, such as transition metal dichalcogenides (TMDs),^{2–6} hexagonal BN,^{7,8} silicene,^{9,10} and germanane,^{10,11} were intensively investigated as candidates for further applications.^{12–15} An appropriate band gap and a superior carrier mobility are essential for excellent performances in nanoelectronics and optoelectronics.^{2,16,17} As for graphene, the most widely studied 2D material so far, the carrier mobility approaches in excess of $200\,000\text{ cm}^2\text{ V}^{-1}\text{ s}^{-1}$.¹⁸ However, lack of a band gap is one of the main obstacles for further applications to field-effect transistors.^{19,20} As a result, many efforts have been devoted to open its band gap.^{21–27} However, the carrier mobility reduced seriously though one

succeeded in increasing the band gap.²⁸ For this reason, it is very urgent to search for a 2D material with both appropriate band gaps and high carrier mobilities.

Recently, MXenes, 2D layered early transition metal carbide, nitride and carbonitride materials, have been prepared by exfoliating MAX phases. The MAX phases with a general formula $\text{M}_{n+1}\text{AX}_n$ ($n = 1–3$), where “M” represents the early d transition metals, “A” represents the main group sp-elements, and “X” represents C and/or N, are a relatively new class of hexagonal structures (space group $P63/mmc$). The bonds between A and M_{n+1}X_n are weaker than those of M–X, and thus chemically more reactive. Therefore, selectively etching only the “A” layers from the MAX phase is possible. To highlight their structural similarity to graphene and the absence of “A”, the new 2D nanosheets are termed as “MXenes”.²⁹ The etching was performed by immersing MAX powders into HF solutions at room temperature.^{29,30} To date, many MXenes such as Ti_2C , V_2C , Nb_2C , Ti_3C_2 , Ta_4C_3 , $(\text{Ti}_{0.5}\text{Nb}_{0.5})_2\text{C}$, $(\text{V}_{0.5}\text{Cr}_{0.5})_3\text{C}_2$ and Ti_3CN have been produced.^{29–32} Due to the use of etching agents, MXenes are always terminated with surface groups such as F, OH and O groups during preparation.³³ O and OH terminated MXenes are the most stable; moreover, at high temperatures, OH groups will be converted into O terminations.³⁴ For this reason, O-terminated MXenes could be prepared in experiments. Most MXenes are metallic with a few exceptions, *e.g.*, Ti_2CO_2 is a semiconductor. Although, there are many computational and experimental investigations

Key Laboratory of Advanced Energy Materials Chemistry (Ministry of Education), Computational Centre for Molecular Science, Institute of New Energy Material Chemistry, Collaborative Innovation Center of Chemical Science and Engineering (Tianjin), School of Materials Science and Engineering, National Institute for Advanced Materials, Nankai University, Tianjin 300071, P.R. China.

E-mail: zhouzhen@nankai.edu.cn

†Electronic supplementary information (ESI) available: Comparison between PBE and HSE results, the structures and carrier mobility of Ti_2CO_2 bilayers, as well as the band structures of nanoribbons. See DOI: 10.1039/c5nr04717j

on MXenes,^{33,35–40} the intrinsic mobility of MXene needs further investigations. Herein, in this work, we investigated the intrinsic mobility of Ti₂CO₂ monolayers and nanoribbons.

2. Computational details

For inorganic semiconductors, the electron coherence length is close to the acoustic phonon wavelength, which is much longer than the bonds. As a result, phonon scattering dominates the intrinsic mobility which can be described by the deformation potential theory.⁴¹ The deformation potential theory has been extensively applied to study the carrier mobility of 2D and one-dimensional (1D) materials.^{28,42–48} For 2D and 1D systems, the analytical expressions for carrier mobility (μ) were derived, respectively.

$$\mu_{2D} = \frac{2e\hbar^3 C}{3k_B T |m^*|^2 E_1^2} \quad (1)$$

$$\mu_{1D} = \frac{e\hbar^2 C}{(2\pi k_B T)^{1/2} |m^*|^{3/2} E_1^2} \quad (2)$$

where T is the temperature, 300 K was adopted in this study, m^* is the effective mass of charge in the transport direction, defined as $m^* = \hbar^2(\partial^2 E(k)/\partial k^2)^{-1}$, and C is the stretching modulus caused by uniaxial strain. In 2D monolayers, C is given by $C = (\partial^2 E_{\text{total}}/\partial \epsilon^2)/S_0$, where E_{total} represents the total energy of a unit cell, ϵ represents the uniaxial strain, S_0 represents the area of the optimized unit cell. E_1 is the deformation potential (DP) constant of valence band maximum (VBM) for holes and conduction band minimum (CBM) for electrons, calculated by using $E_1 = \partial E_{\text{edge}}/\partial \epsilon$. E_{edge} is the energy of VBM or CBM along the transport direction. e is the electron charge, \hbar is the reduced Planck constant, and k_B is the Boltzmann constant.

First-principles computations based on density functional theory (DFT) were performed with a plane-wave technique as implemented in the Vienna Ab initio simulation package (VASP).⁴⁹ The projector augmented wave (PAW) pseudopotential was adopted.⁵⁰ A 550 eV cutoff was used for the plane wave basis set. The exchange–correlation energy was described with the functional of Perdew, Burke, and Ernzerhof (PBE).⁵¹ The DFT-D2 method was adopted to consider the van der Waals force for weak interactions.⁵² The Brillouin zone was represented by Monkhorst–Pack special k -point meshes of $16 \times 16 \times 1$ for monolayers, $16 \times 1 \times 1$ for zigzag nanoribbons and $1 \times 16 \times 1$ for armchair nanoribbons. To avoid any artificial interactions between MXene sheets or nanoribbons and the periodically repeated images, a vacuum space of 20 Å was inserted. As is known to all, generalized gradient approximation (GGA) functional systematically underestimates the band gaps,⁵³ but the effects on the trend of band structures can be ignored. To check it, the band structures of Ti₂CO₂ monolayers were also calculated with the hybrid exchange–correlation functional HSE06.⁵⁴

3. Results and discussion

First, we focused on the structural and electronic properties of Ti₂CO₂ monolayers. The PBE optimized structure of the free-standing Ti₂CO₂ monolayer is shown in Fig. 1 and its first Brillouin zone is shown in Fig. 2a. The calculated band structures from both PBE and HSE06 are shown in Fig. S1† (ESI) and the effective masses calculated with the PBE and HSE06 functionals are shown in Table S1,† which indicates that PBE could give very similar carrier mobilities to HSE06. Moreover, there are several reports in which carrier mobility was calculated with PBE functional.^{42–45,47,48} The band gap computed by using the PBE functional is 0.25 eV as shown in Fig. 2b, which is consistent with previous DFT studies.^{33,55}

Two directions, x and y , were investigated as shown in Fig. 2a. At the band gap wavevector, which is the Γ point, the valence band disperses more strongly than the conduction band, indicating a smaller effective mass for holes than electrons.

To compute the in-plane stiffness C and the DP constant E_1 , the calculated relative energy and the VBM and CBM posi-

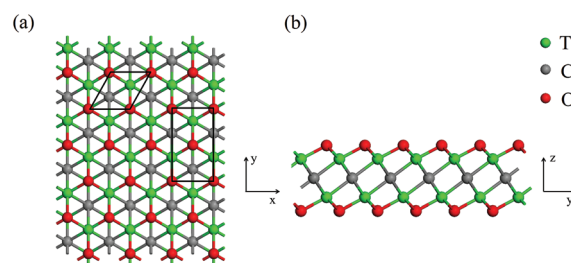


Fig. 1 Geometry of a Ti₂CO₂ monolayer. Right-handed coordination system is used. (a) Top view of the Ti₂CO₂ monolayer. The areas circulated by black lines represent the hexagonal primitive cell and the orthogonal supercell. (b) Side view of the Ti₂CO₂ monolayer.

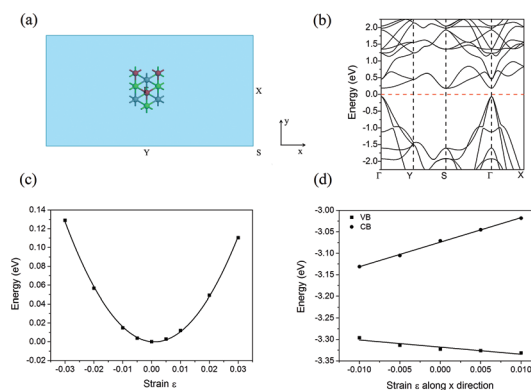


Fig. 2 (a) The first Brillouin zone of an orthogonal supercell. (b) Band structure near the Fermi level for the Ti₂CO₂ monolayer in the orthogonal supercell. (c) The relationship between energy and strain along the x direction. The solid line is a quadratic fitting to the data. (d) The CBM and VBM along the x direction as a function of deformation proportion. The solid lines are linear fittings to the data.

tions of Ti_2CO_2 monolayers as a function of the uniaxial strain ϵ along the x direction are shown in Fig. 2c and d, respectively. Using $C = (\partial^2 E_{\text{total}}/\partial \epsilon^2)/S_0$ and $E_1 = \partial E_{\text{edge}}/\partial \epsilon$, the in-plane stiffness C and the DP constant E_1 could be obtained. On the basis of the obtained $|m^*|$, C and $|E_1|$, calculated by using eqn (1), the carrier mobility of the 2D Ti_2CO_2 monolayer at room temperature ($T = 300$ K) and the relaxation time ($\tau = \mu m^*/e$) are shown in Table 1.

The electron mobility is $6.11 \times 10^2 \text{ cm}^2 \text{ V}^{-1} \text{ s}^{-1}$ along the x direction and $2.54 \times 10^2 \text{ cm}^2 \text{ V}^{-1} \text{ s}^{-1}$ along the y direction, while the hole mobility is $7.41 \times 10^4 \text{ cm}^2 \text{ V}^{-1} \text{ s}^{-1}$ along the x direction and $2.25 \times 10^4 \text{ cm}^2 \text{ V}^{-1} \text{ s}^{-1}$ along the y direction. The carrier mobility along the x direction is about three times higher than that along the y direction, which exhibits high anisotropy in the Ti_2CO_2 monolayers. Moreover, in the x or y direction, the hole mobility is two orders of magnitude higher than the electron mobility. This property can be used in various applications such as the separation of electrons and holes for photocatalysis. These results can be further explained by the wave functions of the band edge state at the Γ point as shown in Fig. S2.† The VBM for holes is quite delocalized along the x and y directions, while the CBM for electrons is localized along the x and y directions.

To investigate the effects of the layer number on the carrier mobility, the Ti_2CO_2 bilayer was considered as shown in Fig. S3 and Table S2.† The results show that the carrier mobility is still high and the huge difference between the hole and electron mobilities and the anisotropy between x and y directions still exist in the Ti_2CO_2 bilayer.

Then, the carrier mobility of armchair Ti_2CO_2 nanoribbons was investigated. Taking $N_a = 16$ as an example, the width of armchair Ti_2CO_2 nanoribbons is defined by the number of Ti and C atoms on the edge of the nanoribbon as shown in Fig. 3a. A series of armchair nanoribbons with width ranging from $N_a = 7$ to 20 were investigated. In 1D nanoribbons, the stretching modulus C is given by $C = (\partial^2 E_{\text{total}}/\partial \epsilon^2)/L_0$, where E_{total} represents the total energy of a unit cell of a nanoribbon, ϵ represents the uniaxial strain applied along the ribbon direction, and L_0 represents the lattice constant of the optimized nanoribbon.

Fig. 4a shows that the stretching modulus C increases monotonously with the width N_a . The calculated deformation potential constant $|E_1|$ of armchair Ti_2CO_2 nanoribbons is shown in Fig. 4b, which displays an oscillating behavior as N_a increases. This might be caused by the edges of nanoribbons.

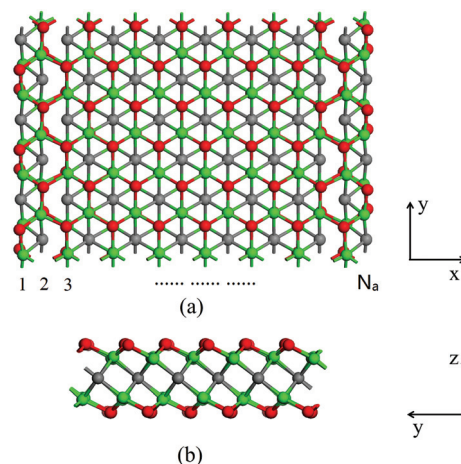


Fig. 3 Optimized geometries of armchair Ti_2CO_2 nanoribbons. (a) Top view of armchair Ti_2CO_2 nanoribbons with width $N_a = 16$. (b) Side view of armchair Ti_2CO_2 nanoribbons.

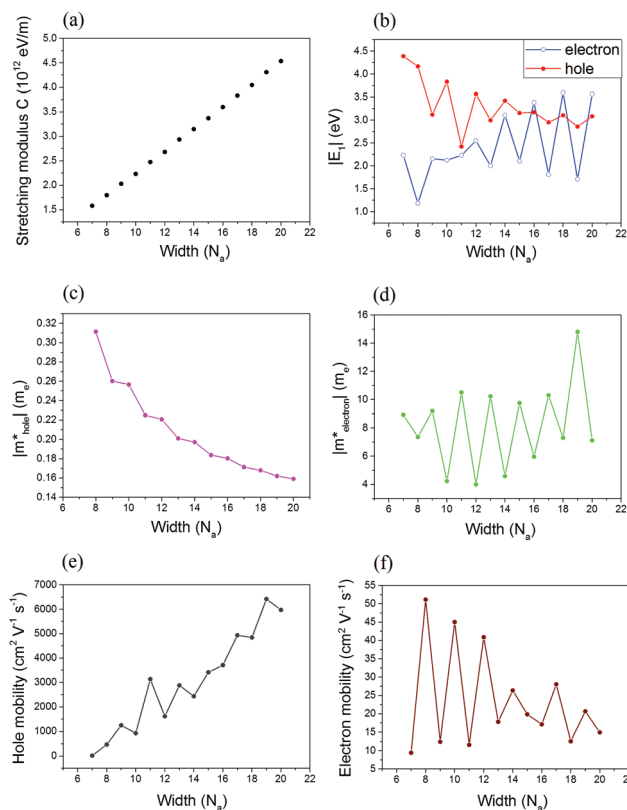


Fig. 4 Electronic properties of armchair Ti_2CO_2 nanoribbons with ribbon width $N_a = 7$ –20: (a) stretching modulus C ; (b) deformation potential constant E_1 ; (c) hole effective mass; (d) electron effective mass; (e) hole mobility and (f) electron mobility for armchair Ti_2CO_2 nanoribbons derived at room temperature (300 K).

Table 1 Effective mass $|m^*|$ (m_e), in-plane stiffness C (N m^{-1}), DP constant $|E_1|$ (eV), carrier mobility μ ($\text{cm}^2 \text{ V}^{-1} \text{ s}^{-1}$) for electrons and holes and relaxation time τ (ps) along the x and y directions in 2D Ti_2CO_2 monolayers

	$ m^* $ (m_e)	C (N m^{-1})	$ E_1 $ (eV)	μ ($\text{cm}^2 \text{ V}^{-1} \text{ s}^{-1}$)	τ (ps)
Electrons (x)	0.44	267.27	5.71	6.11×10^2	0.15
Holes (x)	0.14	267.27	1.66	7.41×10^4	5.74
Electrons (y)	4.53	265.21	0.85	2.54×10^2	0.66
Holes (y)	0.16	265.21	2.60	2.25×10^4	2.01

The edges of nanoribbons with a width of $N_a = 2k$ (k is an integer) are asymmetric as shown in Fig. 3a while the edges are symmetric when $N_a = 2k + 1$.

The calculated effective masses for holes and electrons in the armchair nanoribbons are shown in Fig. 4c and d. The effective mass for holes decreases monotonously with the width N_a . With increasing the width N_a of nanoribbons, the effective mass for holes gradually approaches $0.16m_e$ which is the effective mass for holes in Ti_2CO_2 planar monolayers along the y direction. Unlike this, the effective mass for electrons displays an oscillating behavior as N_a increases. The band gap of the armchair Ti_2CO_2 nanoribbons was also calculated as shown in Fig. S4.† The band gap oscillates and the amplitude decreases gradually.

Calculated by using eqn (2), the hole and electron mobilities μ at room temperature are shown in Fig. 4e and f. Both show an oscillation. In general, the hole mobility presents a rising trend and reaches more than $6000 \text{ cm}^2 \text{ V}^{-1} \text{ s}^{-1}$ when $N_a = 19$. Interestingly, the electron mobility oscillates in the range of $5\text{--}55 \text{ cm}^2 \text{ V}^{-1} \text{ s}^{-1}$ when $N_a = 7\text{--}20$ which is about two orders of magnitude lower than the hole mobility.

In order to explain the dramatic difference between the hole and electron mobilities, taking $N_a = 19$ as an example, the wave functions of the band edge state at the Γ point, *i.e.*, VBM for holes and CBM for electrons were calculated and are shown in Fig. 5. The band structure of armchair Ti_2CO_2 nanoribbons with $N_a = 19$ is shown in Fig. S5.† For VBM, which is responsible for hole transport, it presents a strong overlap of the wave function and the bonding character is connected along the transport direction. Moreover, for CBM, which is responsible for electron transport, the wave function is more localized along the transport direction. As a result, the electron mobility is low. The dramatically different transport properties make it a very promising candidate for future applications to electronics and optoelectronics.

Next, we examined the zigzag Ti_2CO_2 nanoribbons. Similar to the armchair nanoribbons, taking $N_z = 15$ as an example, the width of zigzag Ti_2CO_2 nanoribbons is defined by the number of Ti, C and O atoms on the edges of the nanoribbons as shown in Fig. S6.† Zhao *et al.* reported that some kinds of zigzag Ti_2CO_2 nanoribbons are metallic.⁵⁶ As a result, we only

take into account the stoichiometric zigzag nanoribbons, which are semiconductors, that is to say, $N_z = 3k$ and $3k + 2$ (k is an integer) only.

Fig. 6a shows the calculated stretching modulus C for the zigzag Ti_2CO_2 nanoribbons. Similar to the armchair nanoribbons, C increases monotonously with the width N_z . It can be seen from Fig. 6b that the calculated deformation potential E_1 value for holes decreases gradually. Meanwhile, for electrons, the deformation potential E_1 displays an oscillating behavior and reaches 5 eV when $N_z = 21$.

Fig. 6c and d present the effective mass for holes and electrons. Similar to the armchair nanoribbons, with increasing the width N_z of nanoribbons, the effective mass for holes decreases gradually and the value is close to $0.26m_e$ when $N_z = 21$ as shown in Fig. 6c. Interestingly, for electrons, the effective mass shows a rising trend. However, the value is much lower than the effective mass for electrons of the armchair nanoribbons. The band gap of the zigzag Ti_2CO_2 nanoribbons was also calculated and is shown in Fig. S7.† Unlike the armchair nanoribbons, the band gap of the zigzag nanoribbons decreases gradually.

The hole and electron mobilities (μ) at room temperature for the zigzag nanoribbons are shown in Fig. 6e and f. The hole mobility of the zigzag nanoribbons with a width of $N_z = 6$

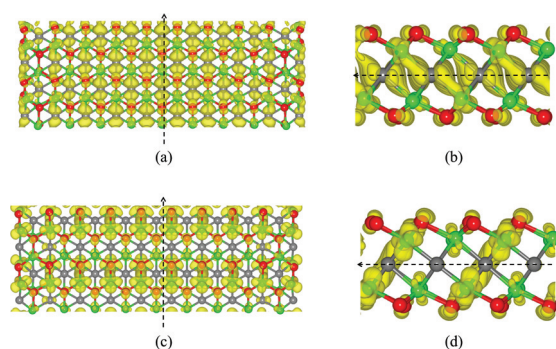


Fig. 5 Spatial structure of wave functions for armchair Ti_2CO_2 with $N_a = 19$ at the Γ point using an isosurface of $0.0008 \text{ e} \text{ \AA}^{-3}$. The black dashed line stands for the stretching direction. The top (a) and side (b) views of VBM. The top (c) and side (d) views of CBM.

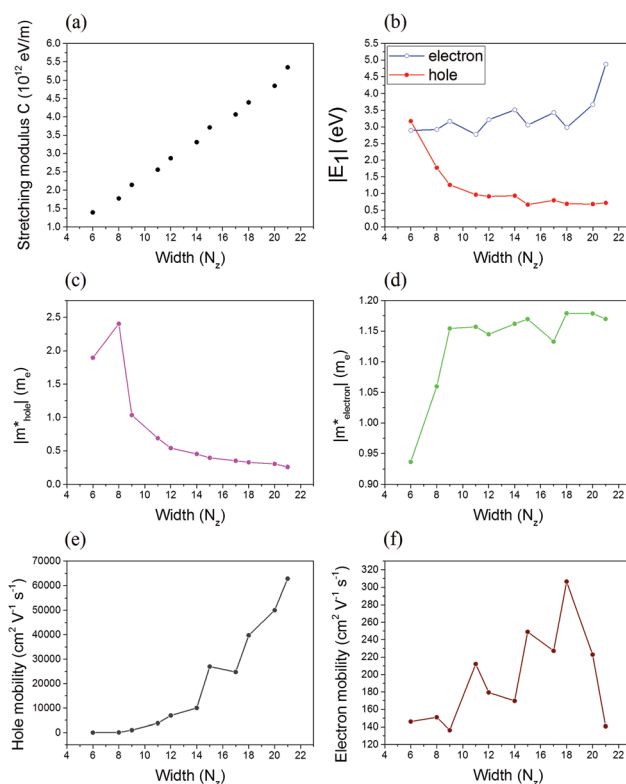


Fig. 6 Electronic properties of zigzag Ti_2CO_2 nanoribbons with ribbon width $N_z = 6\text{--}21$ ($3k$ and $3k + 2$ only): (a) stretching modulus C ; (b) deformation potential constant E_1 ; (c) hole effective mass; (d) electron effective mass; (e) hole mobility and (f) electron mobility for zigzag Ti_2CO_2 nanoribbons derived at room temperature (300 K).

is only $42 \text{ cm}^2 \text{ V}^{-1} \text{ s}^{-1}$. With increasing the width N_z of nanoribbons, the hole mobility increases rapidly. When $N_z = 21$, the hole mobility reaches more than $6 \times 10^4 \text{ cm}^2 \text{ V}^{-1} \text{ s}^{-1}$ which is higher than the value of the zigzag graphene nanoribbons.⁴² The electron mobility of the zigzag nanoribbons shows an oscillation in the range of $120\text{--}320 \text{ cm}^2 \text{ V}^{-1} \text{ s}^{-1}$. Compared with the hole mobility, the width N_z has very little influence on the electron mobility. Similar to the armchair nanoribbons, the dramatic difference between the hole and electron mobilities also exists in the zigzag nanoribbons when $N_z > 11$.

Taking $N_z = 18$ as an example, the wave functions of the band edge state at the Γ point were calculated and are shown in Fig. 7. The band structure of the zigzag Ti_2CO_2 nanoribbons is shown in Fig. S8.† For VBM, which is responsible for hole transport, the wave function along the stretching direction presents a strong overlap. As shown in Fig. 7a, the wider the nanoribbon is, the more overlap exists. As a result, the hole mobility increases rapidly with increasing the width N_z . For CBM, which is responsible for electron transport, the conjugation of Ti atoms at the edge of the nanoribbon makes a major contribution to the electron mobility as shown in Fig. 7c and d. For this reason, compared with the hole mobility, the electron mobility is insensitive to the width N_z .

We found that the dramatic difference between the hole and electron mobilities would exist in both the monolayers and nanoribbons. This property still exists in Ti_2CO_2 bilayers. The results make Ti_2CO_2 a very promising candidate for various applications such as the separation of electrons and holes for photocatalysis. For the nanoribbons, the hole mobility can be controlled by changing the width of the nanoribbons. Moreover, for the zigzag nanoribbons, the atoms at the edge of nanoribbons make a major contribution to the electron mobility. As a result, for further application, the edge engineering in the zigzag Ti_2CO_2 nanoribbons would be used to control the electron mobility to meet the need of various applications.

For graphene, the carrier mobility approaches in excess of $200\,000 \text{ cm}^2 \text{ V}^{-1} \text{ s}^{-1}$. However, lack of a band gap is one of the

main obstacles for further applications. Therefore, MoS_2 has recently been used in field-effect transistors. However, the carrier mobility of monolayered MoS_2 is $200 \text{ cm}^2 \text{ V}^{-1} \text{ s}^{-1}$,¹² improvable to $500 \text{ cm}^2 \text{ V}^{-1} \text{ s}^{-1}$,¹⁷ a value which is orders of magnitude lower than Ti_2CO_2 . In addition to MoS_2 , the electron mobility of Ti_2CO_2 monolayers is much higher than those of many studied 2D materials such as hydrogenated graphene ($105 \text{ cm}^2 \text{ V}^{-1} \text{ s}^{-1}$), fluorinated graphene ($45 \text{ cm}^2 \text{ V}^{-1} \text{ s}^{-1}$), BN ($487 \text{ cm}^2 \text{ V}^{-1} \text{ s}^{-1}$) and BC_2N ($180 \text{ cm}^2 \text{ V}^{-1} \text{ s}^{-1}$),⁴⁴ and the hole mobility of the Ti_2CO_2 monolayer is even higher than the black phosphorus monolayer (phosphorene, $2.6 \times 10^4 \text{ cm}^2 \text{ V}^{-1} \text{ s}^{-1}$)⁴⁶ and the titanium trisulfide monolayer ($1.21 \times 10^3 \text{ V}^{-1} \text{ s}^{-1}$).⁴⁸ Moreover, Ti_2CO_2 has a band gap, high carrier mobility, strongly anisotropic behavior and exhibits huge difference between the hole and electron mobilities. Meanwhile, the imaginary part $\epsilon_2(\omega)$ of the dielectric function for the Ti_2CO_2 monolayers is shown in Fig. S9,† which demonstrates the strong visible-light absorption of Ti_2CO_2 monolayers. As a result, Ti_2CO_2 can be a very promising candidate material in various applications such as nanoelectronic devices and photocatalysts.

4. Conclusion

In conclusion, we have computed the acoustic phonon limited carrier mobility of Ti_2CO_2 monolayers and nanoribbons by using first-principles computations and deformation potential theory. The results indicate that the hole mobility along the x direction can reach $7.41 \times 10^4 \text{ cm}^2 \text{ V}^{-1} \text{ s}^{-1}$, three times as large as the value along the y direction, and exhibits strongly anisotropic behavior. Moreover, the huge difference between the hole and electron mobilities which still exists in the Ti_2CO_2 bilayers and nanoribbons could be used in the separation of holes and electrons for photocatalysis. For nanoribbons, the width controlling and edge engineering would be effective in adjusting the carrier mobility which would make it viable to a wide range of applications in electronics and optoelectronics. More importantly, Ti_2CO_2 nanosheets could be experimentally achieved, though the purity and quality are not high enough for carrier measurements. We would like to invite experimental colleagues to confirm the computational prediction.

Acknowledgements

This work was supported by NSFC (21273118) and the MOE Innovation Team (IRT13022) in China. The computations were performed on Magic Cube at the Shanghai Supercomputer Center.

Notes and references

- 1 K. S. Novoselov, D. Jiang, F. Schedin, T. J. Booth, V. V. Khotkevich, S. V. Morozov and A. K. Geim, *Proc. Natl. Acad. Sci. U. S. A.*, 2005, **102**, 10451–10453.

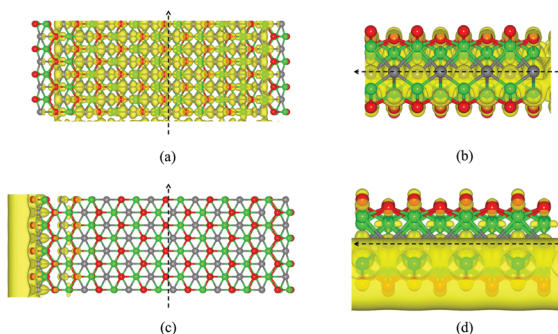


Fig. 7 Spatial structure of wave functions for zigzag Ti_2CO_2 nanoribbons with $N_z = 18$ at the Γ point using an isosurface of $0.001 \text{ e} \text{ \AA}^{-3}$. The black dashed line stands for the direction of stretching. The top (a) and side (b) views of VBM. The top (c) and side (d) views of CBM.

- 2 A. K. Geim and I. V. Grigorieva, *Nature*, 2013, **499**, 419–425.
- 3 Q. H. Wang, K. Kalantar-Zadeh, A. Kis, J. N. Coleman and M. S. Strano, *Nat. Nanotechnol.*, 2012, **7**, 699–712.
- 4 Z. Zeng, Z. Yin, X. Huang, H. Li, Q. He, G. Lu, F. Boey and H. Zhang, *Angew. Chem., Int. Ed.*, 2011, **50**, 11093–11097.
- 5 K.-G. Zhou, N.-N. Mao, H.-X. Wang, Y. Peng and H.-L. Zhang, *Angew. Chem., Int. Ed.*, 2011, **50**, 10839–10842.
- 6 K.-A. N. Duerloo, M. T. Ong and E. J. Reed, *J. Phys. Chem. Lett.*, 2012, **3**, 2871–2876.
- 7 C. Jin, F. Lin, K. Suenaga and S. Iijima, *Phys. Rev. Lett.*, 2009, **102**, 195505.
- 8 H. Zeng, C. Zhi, Z. Zhang, X. Wei, X. Wang, W. Guo, Y. Bando and D. Golberg, *Nano Lett.*, 2010, **10**, 5049–5055.
- 9 P. Vogt, P. De Padova, C. Quaresima, J. Avila, E. Frantzeskakis, M. C. Asensio, A. Resta, B. Ealet and G. Le Lay, *Phys. Rev. Lett.*, 2012, **108**, 155501.
- 10 M. Houssa, E. Scalise, K. Sankaran, G. Pourtois, V. V. Afanas'ev and A. Stesmans, *Appl. Phys. Lett.*, 2011, **98**, 223107.
- 11 E. Bianco, S. Butler, S. Jiang, O. D. Restrepo, W. Windl and J. E. Goldberger, *ACS Nano*, 2013, **7**, 4414–4421.
- 12 B. Radisavljevic, A. Radenovic, J. Brivio, V. Giacometti and A. Kis, *Nat. Nanotechnol.*, 2011, **6**, 147–150.
- 13 Y. Yoon, K. Ganapathi and S. Salahuddin, *Nano Lett.*, 2011, **11**, 3768–3773.
- 14 I. Popov, G. Seifert and D. Tománek, *Phys. Rev. Lett.*, 2012, **108**, 156802.
- 15 F. Xia, D. B. Farmer, Y.-m. Lin and P. Avouris, *Nano Lett.*, 2010, **10**, 715–718.
- 16 E. Hwang and S. D. Sarma, *Phys. Rev. B: Condens. Matter*, 2008, **77**, 115449.
- 17 R. Fivaz and E. Mooser, *Phys. Rev.*, 1967, **163**, 743.
- 18 K. I. Bolotin, K. J. Sikes, Z. Jiang, M. Klima, G. Fudenberg, J. Hone, P. Kim and H. L. Stormer, *Solid State Commun.*, 2008, **146**, 351–355.
- 19 E. H. Hwang and S. Das Sarma, *Phys. Rev. B: Condens. Matter*, 2008, **77**, 195412.
- 20 F. Schwierz, *Nat. Nanotechnol.*, 2010, **5**, 487–496.
- 21 Q. Yan, B. Huang, J. Yu, F. Zheng, J. Zang, J. Wu, B.-L. Gu, F. Liu and W. Duan, *Nano Lett.*, 2007, **7**, 1469–1473.
- 22 M. Han, B. Özyilmaz, Y. Zhang and P. Kim, *Phys. Rev. Lett.*, 2007, **98**, 206805.
- 23 D. Elias, R. Nair, T. Mohiuddin, S. Morozov, P. Blake, M. Halsall, A. Ferrari, D. Boukhvalov, M. Katsnelson and A. Geim, *Science*, 2009, **323**, 610–613.
- 24 E. Bekyarova, M. E. Itkis, P. Ramesh, C. Berger, M. Sprinkle, W. A. de Heer and R. C. Haddon, *J. Am. Chem. Soc.*, 2009, **131**, 1336–1337.
- 25 L. Ci, L. Song, C. Jin, D. Jariwala, D. Wu, Y. Li, A. Srivastava, Z. Wang, K. Storr and L. Balicas, *Nat. Mater.*, 2010, **9**, 430–435.
- 26 M. Yang, L. Zhou, J. Wang, Z. Liu and Z. Liu, *J. Phys. Chem. C*, 2012, **116**, 844–850.
- 27 Y. Zhou, Z. Wang, P. Yang and F. Gao, *J. Phys. Chem. C*, 2012, **116**, 7581–7586.
- 28 J. Wang, R. Zhao, M. Yang, Z. Liu and Z. Liu, *J. Chem. Phys.*, 2013, **138**, 084701.
- 29 M. Naguib, M. Kurtoglu, V. Presser, J. Lu, J. Niu, M. Heon, L. Hultman, Y. Gogotsi and M. W. Barsoum, *Adv. Mater.*, 2011, **23**, 4248–4253.
- 30 M. Naguib, O. Mashtalir, J. Carle, V. Presser, J. Lu, L. Hultman, Y. Gogotsi and M. W. Barsoum, *ACS Nano*, 2012, **6**, 1322–1331.
- 31 M. Naguib, J. Halim, J. Lu, K. M. Cook, L. Hultman, Y. Gogotsi and M. W. Barsoum, *J. Am. Chem. Soc.*, 2013, **135**, 15966–15969.
- 32 F. Chang, C. Li, J. Yang, H. Tang and M. Xue, *Mater. Lett.*, 2013, **109**, 295–298.
- 33 M. Naguib, V. N. Mochalin, M. W. Barsoum and Y. Gogotsi, *Adv. Mater.*, 2014, **26**, 992–1005.
- 34 Y. Xie, M. Naguib, V. N. Mochalin, M. W. Barsoum, Y. Gogotsi, X. Yu, K.-W. Nam, X.-Q. Yang, A. I. Kolesnikov and P. R. C. Kent, *J. Am. Chem. Soc.*, 2014, **136**, 6385–6394.
- 35 Q. Tang, Z. Zhou and P. Shen, *J. Am. Chem. Soc.*, 2012, **134**, 16909–16916.
- 36 Q. Tang and Z. Zhou, *Prog. Mater. Sci.*, 2013, **58**, 1244–1315.
- 37 Z. Ma, Z. Hu, X. Zhao, Q. Tang, D. Wu, Z. Zhou and L. Zhang, *J. Phys. Chem. C*, 2014, **118**, 5593–5599.
- 38 Y. Jing, Z. Zhou, C. R. Cabrera and Z. Chen, *J. Mater. Chem. A*, 2014, **2**, 12104.
- 39 X. Zhang, Z. Ma, X. Zhao, Q. Tang and Z. Zhou, *J. Mater. Chem. A*, 2015, **3**, 4960–4966.
- 40 J. Lei, X. Zhang and Z. Zhou, *Front. Phys.*, 2015, **10**, 276–286.
- 41 J. Bardeen and W. Shockley, *Phys. Rev.*, 1950, **80**, 72–80.
- 42 M.-Q. Long, L. Tang, D. Wang, L. Wang and Z. Shuai, *J. Am. Chem. Soc.*, 2009, **131**, 17728–17729.
- 43 M. Long, L. Tang, D. Wang, Y. Li and Z. Shuai, *ACS Nano*, 2011, **5**, 2593–2600.
- 44 S. Bruzzone and G. Fiori, *Appl. Phys. Lett.*, 2011, **99**, 222108.
- 45 J. Xie, Z. Y. Zhang, D. Z. Yang, D. S. Xue and M. S. Si, *J. Phys. Chem. Lett.*, 2014, **5**, 4073–4077.
- 46 J. Qiao, X. Kong, Z.-X. Hu, F. Yang and W. Ji, *Nat. Commun.*, 2014, **5**, 4475.
- 47 Y. Cai, G. Zhang and Y.-W. Zhang, *J. Am. Chem. Soc.*, 2014, **136**, 6269–6275.
- 48 J. Dai and X. C. Zeng, *Angew. Chem., Int. Ed.*, 2015, **127**, 7682–7686.
- 49 G. Kresse and J. Furthmüller, *Phys. Rev. B: Condens. Matter*, 1996, **54**, 11169.
- 50 G. Kresse and D. Joubert, *Phys. Rev. B: Condens. Matter*, 1999, **59**, 1758.
- 51 J. P. Perdew, K. Burke and M. Ernzerhof, *Phys. Rev. Lett.*, 1996, **77**, 3865.
- 52 S. Grimme, *J. Comput. Chem.*, 2006, **27**, 1787–1799.
- 53 S. Kümmel and L. Kronik, *Rev. Mod. Phys.*, 2008, **80**, 3–60.
- 54 J. Heyd, G. E. Scuseria and M. Ernzerhof, *J. Chem. Phys.*, 2003, **118**, 8207.
- 55 M. Khazaei, M. Arai, T. Sasaki, C.-Y. Chung, N. S. Venkataramanan, M. Estili, Y. Sakka and Y. Kawazoe, *Adv. Funct. Mater.*, 2013, **23**, 2185–2192.
- 56 S. Zhao, W. Kang and J. Xue, *J. Mater. Chem. C*, 2015, **3**, 879–888.